

RESEARCH ARTICLE

10.1002/2017JA024104

Plasma sheet injections into the inner magnetosphere: Two-way coupled OpenGGCM-RCM model results

W. D. Cramer¹ , J. Raeder¹ , F. R. Toffoletto², M. Gilson^{1,3}, and B. Hu^{2,4}¹Space Science Center, University of New Hampshire, Durham, New Hampshire, USA, ²Department of Physics and Astronomy, Rice University, Houston, Texas, USA, ³Pattern Technologies Inc., Mountain View, California, USA, ⁴CGG Services, Houston, Texas, USA

Key Points:

- There is a clear association of plasma sheet injections with bubbles
- The majority of inward plasma transport in the magnetotail beyond geosynchronous orbit is due to bubbles, regardless of storm activity
- The average peak velocity of injections is higher for increasing downtail distances, stronger storms, and storms driven by CIRs

Correspondence to:

W. D. Cramer,
d.cramer@unh.edu

Citation:

Cramer, W. D., J. Raeder, F. R. Toffoletto, M. Gilson, and B. Hu (2017), Plasma sheet injections into the inner magnetosphere: Two-way coupled OpenGGCM-RCM model results, *J. Geophys. Res. Space Physics*, 122, 5077–5091, doi:10.1002/2017JA024104.

Received 1 MAR 2017

Accepted 24 APR 2017

Accepted article online 28 APR 2017

Published online 8 MAY 2017

Abstract Plasma sheet injections associated with low flux tube entropy bubbles have been found to be the primary means of mass transport from the plasma sheet to the inner magnetosphere. This phenomenon has been primarily studied with satellite data and stand-alone ring current models with artificial boundary conditions. This study introduces a new two-way coupling between a kinetic ring current model (Rice Convection Model, or RCM) and a global magnetosphere MHD model (Open Geospace General Circulation Model, or OpenGGCM). Multiple geomagnetic storms and one period of quiet are modeled to track and characterize inward flow behavior. Simulations show that (1) there is a clear association of plasma sheet injections with bubbles, (2) the majority of inward plasma transport in the magnetotail beyond $6.6 R_E$ is due to bubbles, regardless of storm activity, and (3) the average peak velocity of injections is higher for increasing downtail distances, stronger storms (when compared with storms having similar drivers), and storms driven by corotating interaction regions (when compared with coronal mass ejection-driven storms of similar strength).

Plain Language Summary Disturbances in the solar wind, most notably coronal mass ejections from the Sun, impact the plasma environment within the Earth's magnetosphere, the region where Earth's geomagnetic field dominates. This so-called "space weather" transfers energy and plasma into the magnetosphere, which ultimately affects the near-Earth plasma environment, or "inner magnetosphere." Plasma is injected into this region from the nightside magnetosphere, or magnetotail, through a combination of steady and transient injections. There is significant debate about the relative importance of these processes, and the character of the injections themselves. In this study, we use simulations of the global magnetosphere to investigate transient injections to determine their relative importance in transporting plasma into the inner magnetosphere as well as the effect that different types of solar wind disturbances have. We find that transient injections are responsible for the vast majority of the plasma injected into the inner magnetosphere and that the velocity of these injections is dependent on the strength of the geomagnetic storm response and the type of solar wind disturbance.

1. Introduction

The interaction of solar wind transients, such as coronal mass ejections (CMEs) and corotating interaction regions (CIRs), with the magnetosphere is the primary catalysts for geomagnetic storms. Magnetic reconnection at the intersection of the solar wind and planetary magnetic fields at the magnetopause transfers solar wind energy into the magnetosphere [Dungey, 1961] and drives magnetospheric convection. The large-scale dusk-to-dawn convection electric field that is created moves particles from the magnetotail earthward through $E \times B$ drift.

Steady adiabatic convection would require the conservation of flux tube entropy (pV^γ , where γ is the adiabatic constant and V is flux tube volume, defined by the field line integral $\int ds/B$) along drift paths [Erickson and Wolf, 1980]. However, inward propagation of constant-entropy flux tubes would lead to inner magnetosphere pressures that require stronger magnetic fields than what are observed (referred to as the "pressure balance inconsistency"). In reality, flux tube entropy decreases with shorter radial distance.

Rather than smooth isotropic inward drift, injections into the inner magnetosphere from the plasma sheet manifest as narrow high-speed flow bursts [Baumjohann et al., 1990]. These fast flows usually contain regions

of relatively low flux tube entropy, called bubbles, whose inward motion is explained by known plasma instabilities [Pontius and Wolf, 1990]. Bubbles travel inward, slowing (braking) as they go due to decreasing difference with the local flux tube entropy, until they reach a region of similar flux tube entropy [Shiokawa et al., 1997; Kim et al., 2012]. At that point, they experience damped oscillations [Chen and Wolf, 1999; Keika et al., 2009; Panov et al., 2010; Pembroke et al., 2012]. Reconnection in the magnetotail is likely responsible for generating these depleted regions [Birn and Hesse, 1996; Baumjohann, 2002; Ohtani et al., 2004; Semenov et al., 2005; Wolf et al., 2009; Birn et al., 2011].

Flow bursts typically have a width of $1-3 R_E$ [Sergeev et al., 1996; Nakamura et al., 2004], and a time scale of $1-2$ min [Schödel et al., 2001; Ohtani et al., 2004; Runov et al., 2015]. They are generally identified by high inward velocity (above 150 km/s [Huang and Frank, 1986; McPherron et al., 2011; Schmid et al., 2016] or 400 km/s [Baumjohann et al., 1990; Gabrielse et al., 2012]), high local electric field ($V_x B_z > 2$ mV/m [Schödel et al., 2001; Gabrielse et al., 2012]), a leading dipolarization front [Liu et al., 2014; Yao et al., 2015; Schmid et al., 2016], and trailing bubble [see Yang et al., 2011, Figure 10]. Flow bursts typically travel in a sunward direction, so those that are distant from midnight local time diverge to the dusk and dawn flanks [Juusola et al., 2011].

Moderately fast inward flows ($V > 100$ km/s) whose speed exceeds the flow burst minimum cutoff at least once are known as bursty bulk flows (BBFs). BBFs have been found to be the source of most earthward plasma transport [Angelopoulos et al., 1992, 1994] and ring current energy within geosynchronous orbit [Yang et al., 2015]. However, only a small portion have been found to penetrate to geosynchronous orbit [Dubyagin et al., 2011; Yu et al., 2014].

The impact of these flow bursts on the inner magnetosphere is under active investigation by the space physics community. Most simulation studies have used models that rely on pure MHD or stand-alone ring current models with artificial boundary conditions. Studies utilizing MHD have investigated the trigger [Ohtani et al., 2004; Birn et al., 2011; Ge et al., 2011; Wiltberger et al., 2015], propagation [Birn et al., 2004], and braking [Wolf et al., 2012] of plasma sheet injections. Stand-alone ring current models have been used to study the effect of impulsive flow bursts on the ring current [Lemon et al., 2004; Zhang et al., 2008; Yang et al., 2015, 2016] and their dynamics [Wolf et al., 2009; Yang et al., 2011, 2012].

In recent years, there has been an effort to couple global MHD models to ring current models. This is necessary in order to get realistic ring current pressures and to ensure that the electric and magnetic fields are computed self-consistently [Glocer et al., 2013]. One-way couplings [Toffoletto et al., 2004; Fok et al., 2006; Moore et al., 2008; Buzulukova et al., 2010; Hu et al., 2010], where MHD parameters are used to determine ring current model boundary conditions, and two-way couplings [de Zeeuw et al., 2004; Pembroke et al., 2012; Glocer et al., 2013; Meng et al., 2013; Yu et al., 2014; Welling et al., 2015] have been used to study magnetospheric phenomena. Pembroke et al. [2012] used a coupled LFM-Rice Convection Model (RCM) to study the magnetic field oscillations in the inner magnetosphere caused by low entropy flow channels. Yu et al. [2014] used BATS-R-US (Block-Adaptive-Tree Solar-wind Roe-type Upwind Scheme) coupled with the RAM-SCB (Ring current-Atmosphere interactions Model with Self-Consistent magnetic field) [Zaharia et al., 2008] to conclude that substorm-associated injections are necessary for ring current strengthening. In this study, we use a different two-way coupled model to investigate the properties of plasma sheet injections as they propagate toward the inner magnetosphere.

2. Model

2.1. OpenGGCM

The OpenGGCM is a global magnetosphere model that uses a semiconservative form of the MHD equations [Raeder et al., 2008] to move a single-fluid plasma through cells of a 3-D, stretched Cartesian grid. The equations are defined such that plasma energy, not total energy, is conserved (see equations (1)–(8), where ρ , v , p , j , B , E , σ , and e represent mass density, velocity, pressure, current density, magnetic field, electric field, conductivity, and plasma energy density, respectively). It uses an explicit second-order predictor-corrector finite difference scheme for advancing the equations in time and a hybrid flux-limited first/fourth-order scheme for spatial discretization.

$$\frac{\partial \rho}{\partial t} = -\nabla \cdot (\rho \vec{v}) \quad (1)$$

$$\frac{\partial \rho \vec{v}}{\partial t} = -\nabla \cdot (\rho \vec{v} \vec{v} + p \underline{\underline{1}}) + \vec{j} \times \vec{B} \quad (2)$$

$$\frac{\partial e}{\partial t} = -\nabla \cdot (\{e + p\} \vec{v}) + \vec{j} \cdot \vec{E} \quad (3)$$

$$\frac{\partial \vec{B}}{\partial t} = -\nabla \times \vec{E} \quad (4)$$

$$\nabla \cdot \vec{B} = 0 \quad (5)$$

$$\vec{E} = -\vec{v} \times \vec{B} + \frac{1}{\sigma} \vec{j} \quad (6)$$

$$\vec{j} = \nabla \times \vec{B} \quad (7)$$

$$e = \frac{\rho v^2}{2} + \frac{p}{\gamma - 1} \quad (8)$$

The OpenGGCM calculates the ionosphere potential using the conductance and field-aligned currents determined by the Coupled Thermosphere Ionosphere Model (CTIM). CTIM models the chemical and photochemical reactions in the upper atmosphere, primarily using the inputs of solar radiation and auroral precipitation (for more information, see *Fuller-Rowell et al. [1996]* and *Raeder et al. [2008]*).

For this study, the MHD grid is 481 cells covering between -35 to $5000 R_E$ in the GSE x coordinate and 180 cells covering -48 to $48 R_E$ in both the GSE y and z coordinates, with smaller widths in the inner magnetosphere region (down to $0.167 R_E$ in x and $0.25 R_E$ in y and z). The inner MHD boundary is set at $2 R_E$. The ionosphere grid is comprised of 361 by 120 cells in magnetic latitude and longitude, respectively. OMNIWeb data are used as input to the model unless it contains any large data gaps, in which case Wind data are used.

2.2. Rice Convection Model

The Rice Convection Model (RCM) [*Toffoletto et al., 2003*] is a ring current model that solves for the motion of plasma flux tubes due to ionosphere potential and magnetic induction and drift forces. It assumes an isotropic particle distribution and includes electrons and protons of various energies that are defined by an energy invariant and flux tube volume. This energy invariant is defined by equation (9), where λ_k is the energy invariant, W_k is the particle energy for species k , and V is the flux tube volume given by $\int ds/B$. All RCM equations assume an adiabatic constant, γ , of 5/3.

$$|\lambda_k| = W_k V^{\frac{2}{3}} \quad (9)$$

The RCM maintains ring current flux tube content in a 2-D ionospheric grid that represents the foot points of the flux tubes. The grid covers a ring in SM coordinates of all longitudes and a range of latitudes between 45 and 82° in the Northern Hemisphere. The grid spacing in latitude is denser at lower latitudes. The RCM derives precipitation from electron density and field-aligned currents from the ring current pressure distribution [*Vasyliunas, 1970; Wolf, 1983*]. It requires input of external plasma boundary conditions, ionosphere potential, and local magnetic fields. Particle losses due to charge exchange are estimated from the sunspot number.

Electron precipitation intensity is calculated from the sum of one quarter of the total electron intensity in each invariant energy bin. Field-aligned currents are calculated from the Vasyliunas equation [*Vasyliunas, 1970*].

2.3. Model Coupling

MHD equations do not adequately represent the physics of the inner magnetosphere, so the RCM is employed to model that region and give feedback to the OpenGGCM, for self-consistency.

Figure 1 shows the coupling interfaces between the models. The OpenGGCM passes MHD pressure and density to the RCM to initialize the ring current plasma population and, in subsequent execution cycles, set the boundary conditions. After execution, the RCM returns the calculated pressure and density in its domain to the OpenGGCM. These values are then used to nudge the MHD values toward those provided by the RCM.

The ionosphere and RCM models exchange plasma information by interpolating values from their respective 2-D grids. Ionosphere potential is provided to the RCM model, and precipitation and field-aligned current information is returned. Prior to recalculating the ionosphere potential, the RCM precipitation and field-aligned currents are blended with those calculated by the OpenGGCM. In the case of auroral precipitation, the RCM quantities are used in low magnetic latitudes associated with the RCM domain, and MHD quantities

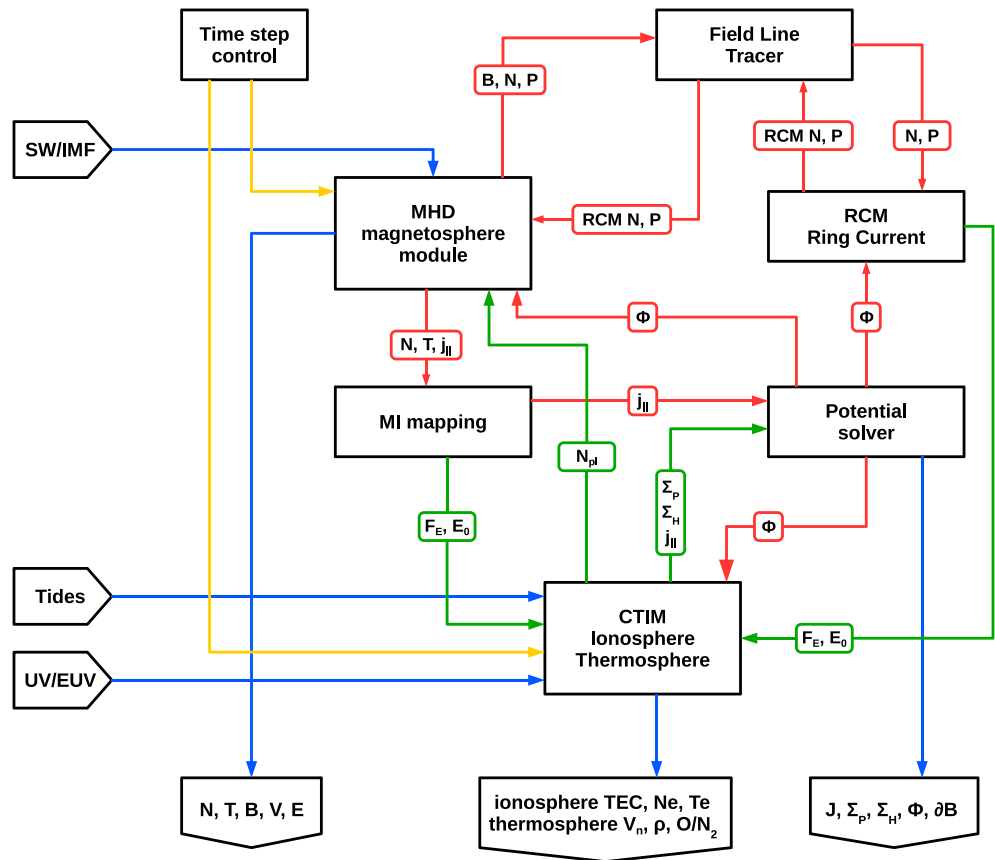


Figure 1. Diagram of OpenGGCM-CTIM-RCM coupling methodology. N , T , V , E , and B are the plasma density, temperature, velocity, electric field, and magnetic field, respectively. The field aligned current is $j_{||}$, Φ is the ionosphere potential, F_E and E_0 are the energy flux and mean energy of precipitating electrons, Σ_H and Σ_P are the ionosphere Hall and Pedersen conductances, and ∂B is the ground magnetic perturbation.

are used at latitudes above that. Field-aligned currents can be blended in a similar manner; however, for this study, MHD currents are used.

More details about the coupling methodology can be found in Appendix A.

3. Event Selection

One quiet period and eight storms of various intensities and solar wind drivers were simulated. Table 1 lists the date, driver, and minimum Dst^* for these events. Dst^* is based on values given by Fenrich and Luhmann [1998]. Four storms driven by a coronal mass ejection (CME) and four that were driven by a corotating interaction region (CIR) were chosen.

Table 1. List of Modeled Storms

ID	Driver	Date	Minimum Dst^* (nT)
Q1	—	1/19/2014	—
I1	CIR	8/5/2013	-41
I2	CIR	6/6/1998	-46
I3	CIR	5/2/2010	-71
I4	CIR	2/27/1997	-86
M1	CME	5/1/2013	-54
M2	CME	5/29/2010	-60
M3	CME	7/15/2012	-105
M4	CME	10/28/2001	-137

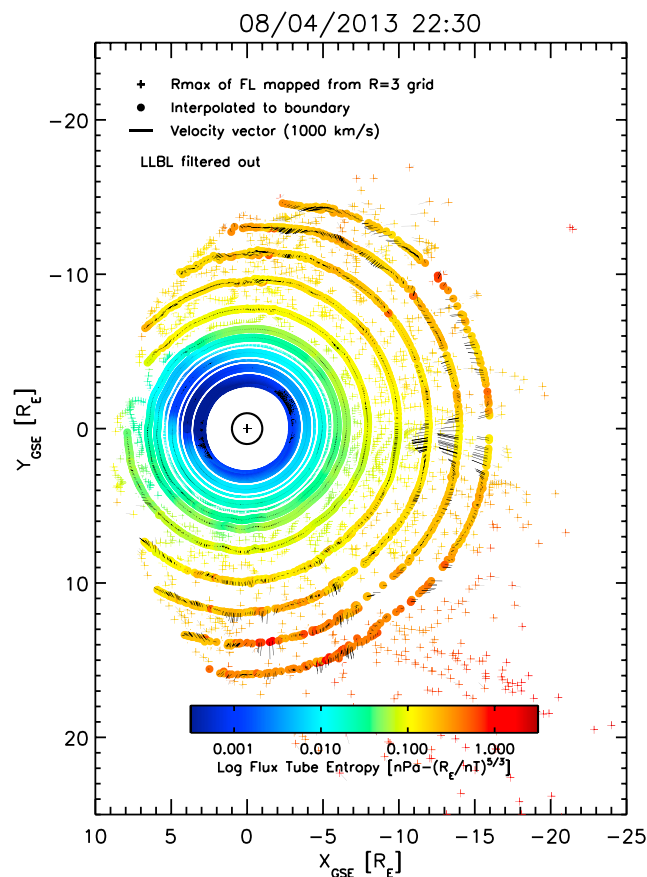


Figure 2. Flux tube entropy and plasma velocity at positions on the current sheet, projected into the GSE X-Y plane, at 2230 UT during the simulated August 2013 storm. Colored symbols and black lines represent the entropy values and velocity vectors, respectively. Plus symbols represent the intersection points of field lines traced from a spherical grid at $3 R_E$. Filled circles represent current sheet values interpolated to various spherical boundaries.

4. Results

4.1. Identification of Injections in Simulation Data

In this study, we look for injection signatures at the current sheet within the nightside plasma sheet. The current sheet is found by tracing magnetic field lines from each tile on a spherical grid $3 R_E$ above the Earth. Each tile covers one degree in both latitude and longitude. Where field lines map to both hemispheres, they are considered closed, and the flux tube volume line integral is calculated. The point on each field line with the farthest radial distance is considered to be the intersection with the current sheet. MHD quantities (pressure, velocity, density, and magnetic field) are extracted from these points. Values along the current sheet, which forms a 2-D surface, are then interpolated to spherical boundaries of various distances (4, 5, 6, 6.6, 8, 10, 12, 14, and $16 R_E$) that cover the region of interest.

Figure 2 shows an example of this procedure. The GSE X-Y coordinates of the points of intersection with the current sheet are shown as “plus” symbols, with associated velocity vectors (black lines) and flux tube entropy values (color) at those locations. Filled circles and associated lines and colors represent those values interpolated to the spherical boundaries. In order to confine the analysis to the inner magnetosphere and plasma sheet regions, closed field lines in the low-latitude boundary layer (LLBL) are filtered out by using a combination of temperature-to-density (T/n) ratio (as in *Tsyganenko and Mukai [2003]*), azimuthal velocity at the outer boundary, and proximity to the boundary. LLBL plasma is cooler and denser than plasma sheet plasma, so *Tsyganenko and Mukai [2003]* identified the plasma sheet as regions where T/n was greater than or equal to a fixed value of 5 keV cm^3 . We find that a fixed value of T/n does not work consistently well for all levels of activity, due to a general storm time increase in temperature and decrease in density at each boundary. At the nightside $10 R_E$ equatorial boundary, the average T/n values vary from about 3 keV cm^3 in quiet periods to $40\text{--}80 \text{ keV cm}^3$ during the storm main phases. A trial-and-error examination of many time steps of the various

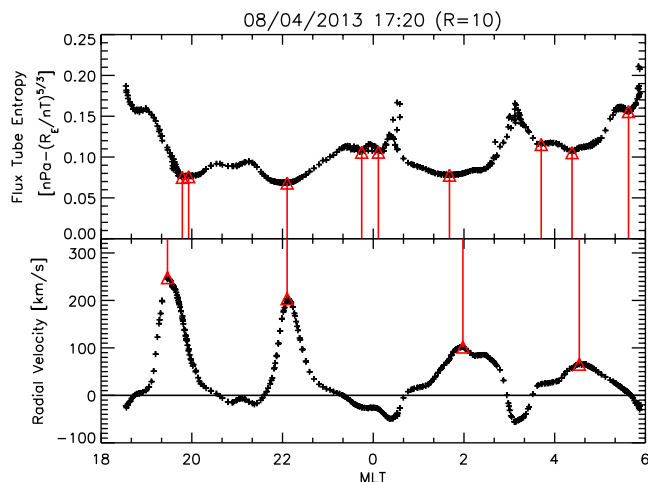


Figure 3. Magnetic local time (MLT) dependence of earthward radial velocity and flux tube entropy at the $10 R_E$ boundary at 1720 UT on 4 August 2013. Automatically determined inward velocity maxima and entropy minima are marked with red triangles and red lines to highlight their frequent collocation.

storms led to a criterion for LLBL plasma of equatorial T/n less than 1.5 times the square root of the nightside average of $T(\text{keV})/n(\text{cm}^{-3})$ at the $10 R_E$ boundary. This corresponds with cutoff values of approximately 2.5 keV cm^3 and $9\text{--}14 \text{ keV cm}^3$ for the average T/n values given above. Although unusual, this relation had the most success at consistently identifying data points in the LLBL. These data points are removed from analysis if they also have tailward velocity and are at the magnetic local time extreme of the nightside closed field line region. The plasma sheet boundary layer can also contain closed field lines, but the effect on our results is minimal as the plasma motion is typically field aligned.

The figure shows a plasma sheet injection near midnight local time that covers the $12\text{--}16 R_E$ boundaries. Flux tube entropy at the injection location is clearly lower than the adjacent values, as indicated by the yellow color. At this particular simulation time, the region of closed field lines does not extend far beyond the $16 R_E$ boundary on the dawnside of midnight but does on the duskside. In general, the flux tube entropy is lower at radial boundaries that are closer to the earth.

The current sheet intersection with a spherical boundary forms an undulating line in magnetic local time (MLT). Figure 3 shows the flux tube entropy (top) and inward radial speed (bottom) on the current sheet at the $10 R_E$ boundary at one moment during the main phase of the August 2013 storm. Local inward velocity maxima at the boundary are the central peaks of individual injections, and local flux tube entropy minima are bubbles. Both bubbles and injection peaks are identified on the figure by red symbols and lines. Numerous examples of collocation of the two phenomena can be seen, indicating a possible relationship.

4.2. Inward Flow and Low Flux Tube Entropy

Figure 4 shows the time series of the local time locations of injections and bubbles shown in Figure 3 for the entire storm main phase. The format is slightly different, with the x axis representing simulation time, the local time on the y axis, and speed represented by color. As before, it shows the nightside injections at a distance of $10 R_E$ during the simulated August 2013 (I1) geomagnetic storm. Figure 4 (first panel) shows actual (black line) and simulated (red line) Dst^* . Actual Dst^* is calculated using the method described by Fenrich and Luhmann [1998], while simulated Dst^* is calculated from Biot-Savart integration of currents in the ring current domain. Figure 4 (second and third panels) shows solar wind dynamic pressure and the GSE Z component of the interplanetary magnetic field, respectively. Figure 4 (fourth panel) shows both the local inward velocity maxima and flux tube entropy minima from 3 h prior to the main phase of the storm to 1 h after. The colored symbols represent the location of the velocity maxima, where color represents the speed, and the black symbols represent flux tube entropy minima, or bubbles. Velocity peaks are usually inward (represented by circular symbols) but can be outward (represented by crosses). The storm main phase start and end times are marked with solid vertical lines. The figure shows a clear correlation between bubbles and injections during the event, especially after the early main phase. Both tend to move toward the flanks over time, occasionally having short bursts of high inward velocity.

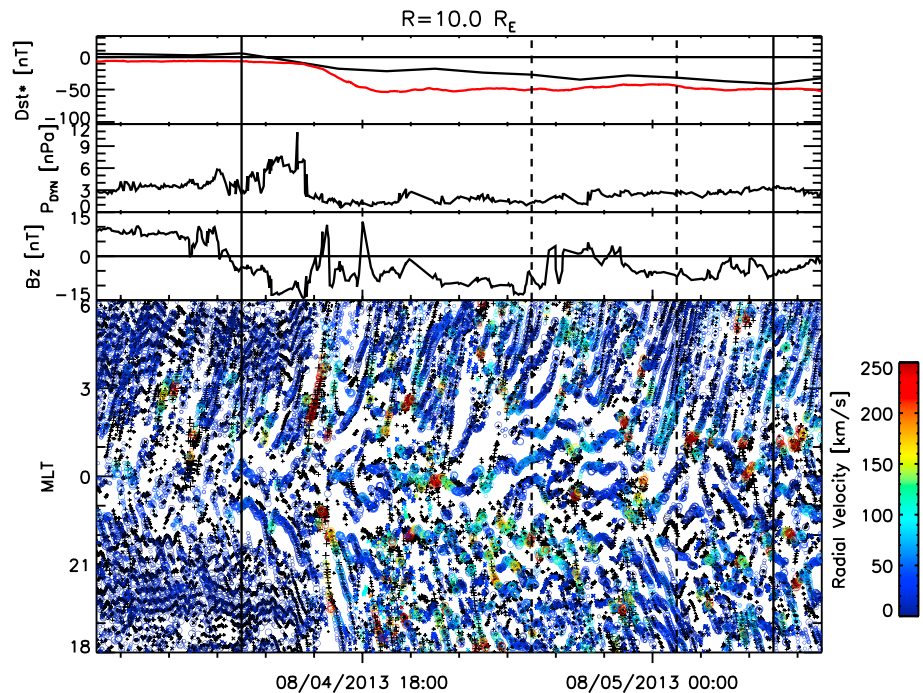


Figure 4. Time series of velocity maxima and flux tube entropy minima in the current sheet (as identified for one time step in Figure 3) at $10 R_E$ during the main phase of the simulated 4 August 2013 storm (I1). (first to third panels) Dst^* (with simulated Dst^* in red), solar wind dynamic pressure, and the z component (GSE) of interplanetary magnetic field, respectively. (fourth panel) The magnetic local time location of inward velocity maxima (colored symbols, where color represents speed) and flux tube entropy minima (plus symbols). The solid vertical lines bracket the storm main phase. The segment between the dashed vertical lines is expanded in Figure 5.

Figure 5 shows a 3 h segment of the same simulated storm (indicated in Figure 4 by dashed lines). From this plot, it is clear that the injection peaks are closely collocated with local flux tube entropy depletions. For this study, injections that are within 20 min of magnetic local time (MLT) of a bubble are considered to be collocated. This angular distance was arrived at by visually analyzing the time series results of using different values and determining which appeared to be more accurate at correctly matching bubbles and inward flow peaks. Collocation is indicated on the plot by colored symbol size, where large circles show collocation.

For this storm, injections near local midnight tend to remain at the same local time, while those on the duskside or dawnside of midnight tend to move toward their respective flank. This is a common feature for all simulated events. Occasionally, the injections reach flow burst speeds (represented by redder colors).

Figure 6 shows injections during a three hour segment of the simulated quiet period on 19 January 2014. Deep entropy minima and high-velocity flow bursts appear to be rare compared to storm times. This is likely due to the much less frequent occurrence of reconnection, which is the probable cause of low flux tube entropy regions. The bubble injection peak collocation is also clear in this sample, although it is less apparent on the flanks than the storm time example.

Figure 7 shows the percentage of injections that are collocated with bubbles during the main phase of all eight storms and the quiet period at the spherical boundaries specified in section 4.1. For all storm main phases at boundaries of $8 R_E$ and beyond, approximately 70–80% of inward flow peaks are collocated with bubbles. At geosynchronous orbit ($6.6 R_E$), a majority of injections are associated with bubbles for seven of the eight storms. There is no apparent relationship to storm driver, but the percentage does generally increase with storm strength (based on minimum Dst^*). At successively closer boundaries, this percentage becomes lower. Presumably, this can be explained by the greater effects of magnetic drift, including gradient, curvature, and $E \times B$ drift, closer to Earth. Beyond $8 R_E$, inward drift due to local flux tube entropy depletion appears to dominate.

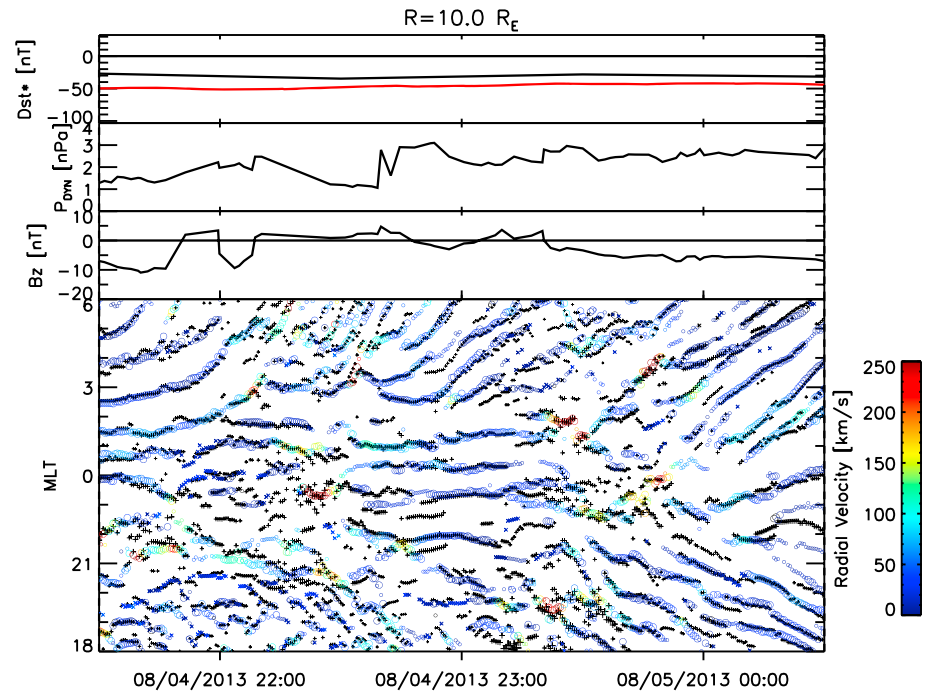


Figure 5. Expanded 3 h segment of Figure 4.

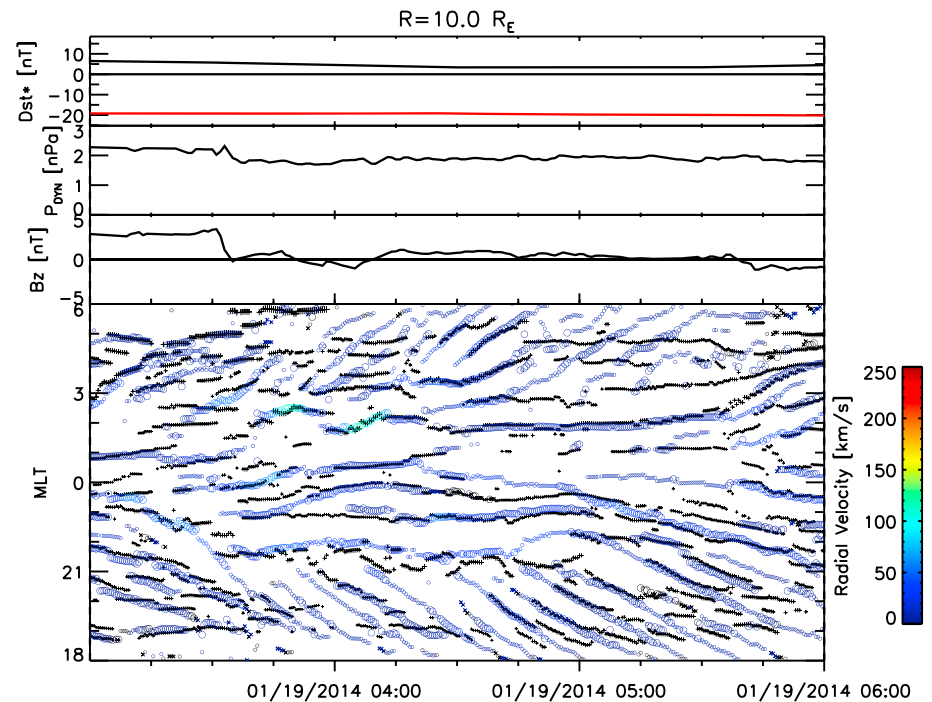


Figure 6. Time series of velocity maxima and flux tube entropy minima in the current sheet at $10 R_E$ during a 3 h segment of the simulated quiet period (Q1). The format is identical to that of Figure 4.

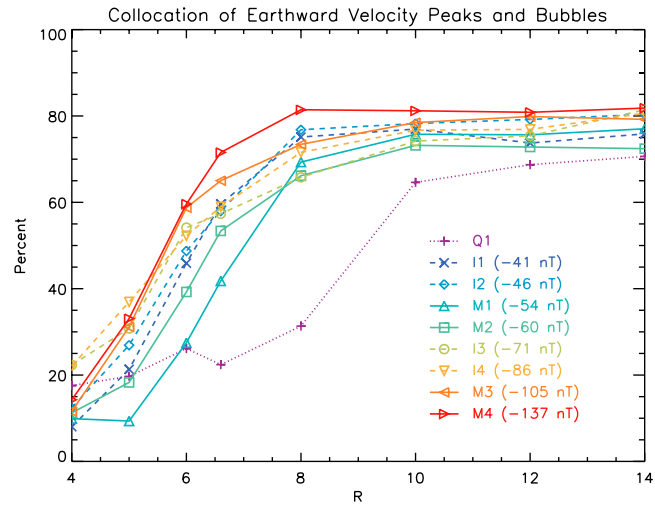


Figure 7. Percentage of inward velocity maxima that are within 20 min of local time of flux tube entropy minima for all simulations and boundaries. Boundary values are connected with solid lines for CME-driven storms, dashed lines for CIR-driven storms, and a dotted line for the quiet period. The colors represent the storm strength order, based on minimum Dst^* (blue is weakest, and red is strongest).

The results for the simulated quiet time is different than that of the eight different storms. Between 6.6 and 12 R_E , the collocation percentage is significantly less than that of the storm main phases. As seen in both Figure 6 and the prestorm time shown in Figure 4, the primary divergences between the injections and bubbles appear to occur in the flank regions. In those instances, the flux tube entropy generally remains at a particular local time, while the injections move further toward the flanks. This is a common feature for nonstorm periods in the simulations. The likely cause of this divergence is the drop-off in flux tube entropy toward the flanks in quiet times, which prevents the bubbles from continued motion in that direction. The injections continue to move in local time due to other magnetic drift forces.

4.3. Plasma Transport

In order to determine the relative contribution of bubbles to inward plasma transport, the inward number flux density (nV_{radial}) of injections is integrated along the nightside current sheet boundary intersection line separately for those that are collocated with bubbles and those that are not. This method essentially assumes

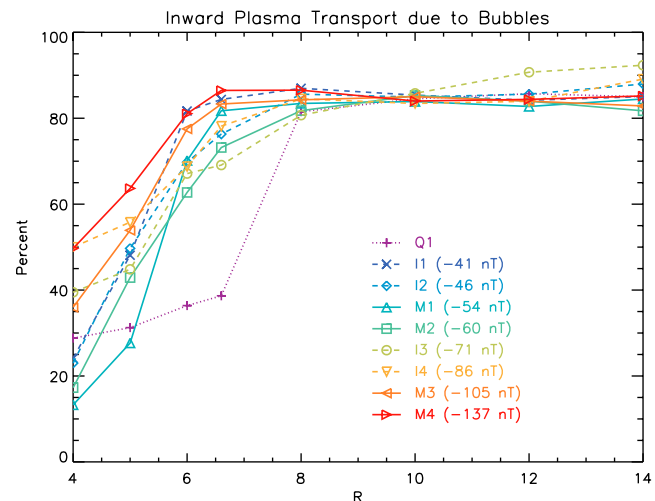


Figure 8. Percentage of total plasma transport across boundaries that is collocated with bubbles for all simulations and boundaries. Boundary values are connected with solid lines for CME-driven storms, dashed lines for CIR-driven storms, and a dotted line for the quiet period. The colors represent the storm strength order, based on minimum Dst^* (blue is weakest, and red is strongest).

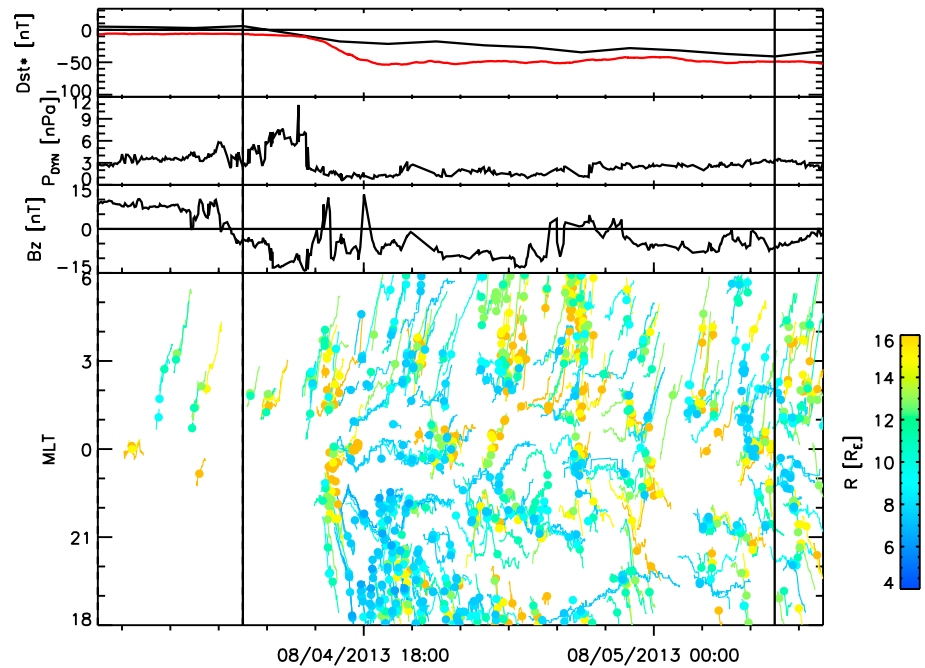


Figure 9. Individual flow burst injections during the main phase of the simulated 4 August 2013 storm (I1). (first to third panels) Dst^* (with simulated Dst^* in red), solar wind dynamic pressure, and the z component (GSE) of interplanetary magnetic field, respectively. (fourth panel) The magnetic local time location of individual injections at all boundaries (R is represented by color, where blue is the innermost and red the outermost). The solid circle represents the time and location of the maximum inward velocity for each injection. The vertical solid lines bracket the storm main phase.

consistent geometry for the flux tubes at a particular boundary. This is not explicitly true, as the dipolarization associated with inward bubble flow tends to make those field lines slightly longer. However, this should only lead to a small underestimation of the plasma transport due to bubbles.

Figure 8 shows the percentage of the total inward transport for all events and quiet time. It shows that above $8 R_E$ for all storm events, approximately 80% of inward plasma transport is due to bubbles. Moving inward below $8 R_E$, that percentage for weaker storms drops off. At geosynchronous orbit, the fraction is still at least two thirds for all storms. Below $6 R_E$, inward transport from bubbles for the stronger storms becomes less important. For the quiet period, the percentage is also about 80% beyond $8 R_E$ but drops more rapidly than for storms inward of that point. As with bubble collocation with injections, this can be explained by the greater strength of magnetic drift forces in the inner magnetosphere.

4.4. Individual Injections

In Figures 4–6, discrete injections can be seen by following the time series of velocity maxima. Their initial appearance, movement in local time (usually toward the flanks), and disappearance can be seen. Figure 9 shows only the discrete injections during the main phase of the August 2013 storm that can be classified as BBFs; i.e., they have peak velocities that exceed a flow burst speed. These discrete injections are identified using an automated process. In this study, the flow burst speed is a function of the boundary distance, defined by equation (10), which is approximately 5 times the average injection speed at each boundary. This variable cutoff is used to account for reduced speeds due to braking as the flow moves inward. The lines on the figure represent the local time location of the injection as a function of time, and the different colors represent boundary distance. The filled circles show the time of maximum inward velocity.

$$v_{fb,min} = \min(30, (R [R_E] - 5) \times 30) \text{ (km/s)} \tag{10}$$

Figure 10 shows the average peak velocity of all injections at each boundary during the storm main phases and the quiet period. As would be expected due to flow braking, the values are larger for more distant boundaries. The increase is approximately linear between $6 R_E$ and $12 R_E$ and levels off inward and outward of that range. Some dependence on storm strength is apparent for storms with a similar driver. CIR-driven storms also have higher injection velocities than CME-driven storms of similar strength.

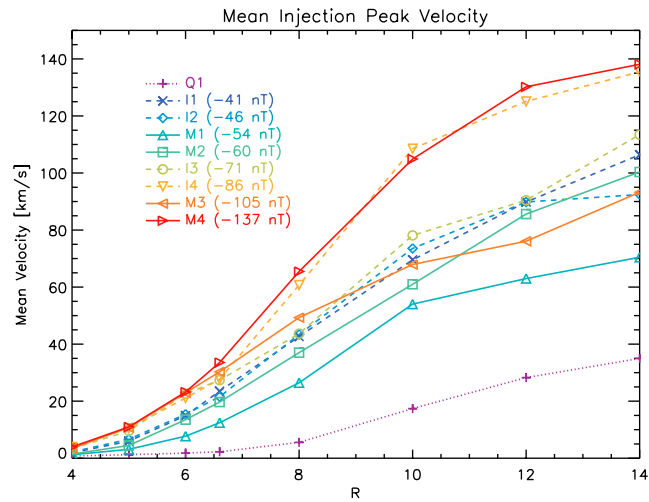


Figure 10. The mean peak velocity of individual injections for all simulations and boundaries. Boundary values are connected with solid lines for CME-driven storms, dashed lines for CIR-driven storms, and a dotted line for the quiet period. The colors represent the storm strength order, based on minimum Dst^* (blue is weakest, and red is strongest).

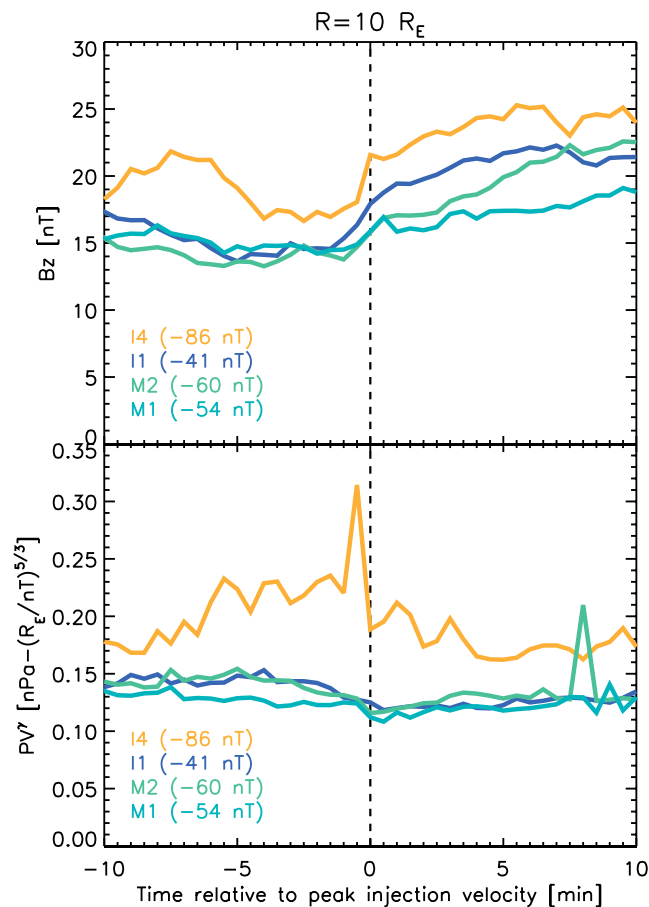


Figure 11. Superposed epoch of B_z and flux tube entropy at the $10 R_E$ boundary for BBFs, based on the time of maximum inward velocity. The colors represent the storm strength order, based on minimum Dst^* (blue is weakest, and red is strongest).

5. Injection Profile

Satellite observations of flow bursts have shown a typical profile of magnetic field, flux tube entropy, and plasma parameters as they move inward [Yang *et al.*, 2011; Runov *et al.*, 2011]. The sequence of observations is that of a high flux tube entropy island, a dipolarization front, and then a low entropy bubble. An increase in B_z indicates that formerly stretched field lines have become more dipolar. The passage of the bubble is indicated by a decrease in flux tube entropy.

Using the time of peak velocity as the reference point, we performed a superposed epoch analysis of the BBFs for four simulations of geomagnetic storms to determine if the mechanism of bubble creation in the model matched that of observations. Figure 11 shows the results for B_z and flux tube entropy. For all four storm main phases, a dip in B_z is observed prior to the peak velocity point. After that time, B_z is observed to be larger. This agrees with the profile shown by Yang *et al.* [2011], where the time of peak velocity is coincident with the passage of the dipolarization front.

Figure 11 (bottom row) shows the flux tube entropy profile in the simulations. Again, the decrease in entropy after the passage of the dipolarization front agrees with the observation-based profile. However, the increase in entropy that corresponds with the leading high entropy island is only clearly seen in one of the simulation results. The reason for the absence of this feature in three of the storms may be due to their relative weakness (in terms of minimum Dst^*). In weaker storms, slower injection velocities may prevent a significantly compressed region at the leading edge from forming. Another possibility is that the high entropy island is narrow enough in the radial direction that it moves through the boundary in a time frame much shorter than the simulation 30 s output cadence.

6. Discussion

This study continues the investigation into plasma sheet injections by creating a new coupling between a global magnetosphere MHD model and an inner magnetosphere model. The OpenGGCM-RCM coupled model is shown to reproduce injection signatures seen in observations. Other coupled models, such as those developed by Pembroke *et al.* [2012] and Yu *et al.* [2014], have also been used to investigate the affect of injections on the ring current, but none have been used to focus in detail on the injections themselves.

We confirm previous findings that the majority of plasma transport into the inner magnetosphere is due to bubbles. However, contrary to previous findings [Dubyagin *et al.*, 2011; Yu *et al.*, 2014], we are able to frequently detect bubble injections that propagate deeper than geosynchronous orbit.

7. Summary and Conclusions

The main findings of this study are as follows:

1. *There is a clear association of plasma sheet injections with bubbles.* At magnetotail distances of $8 R_E$ or greater during storm main phase and $10 R_E$ during a quiet period, the vast majority of inward flow peaks exist alongside bubble depletions, even where these depletions are slight compared to neighboring values. Moving inward of the aforementioned boundaries, the association of injections with bubbles drops off rapidly. This is more pronounced for nonstorm times, in which case bubbles, but not the injections, appear to stall as they move into the flanks due to lower flux tube entropy in those regions. In those cases, injections continue to move toward the flanks due to magnetic drift forces.
2. *The majority of inward plasma transport in the magnetotail beyond $6.6 R_E$ is due to bubbles, regardless of storm activity.* Beyond distances of $6 R_E$ during storm main phase and $8 R_E$ during a quiet period, over two thirds of the plasma transport is associated with bubbles. During the main phase of storms, approximately 80% of the inward number flux density at the $8 R_E$ and beyond is associated with bubbles, regardless of storm driver or strength. Within $8 R_E$, this percentage begins to drop off at a boundary distance that is roughly dependent on storm strength, with stronger events maintaining the high percentage further inward.
3. *The average peak velocity of injections is dependent on boundary distance, storm driver, and storm strength.* The average peak inward velocity for all injections decreases approximately linearly with decreasing boundary distance and tends to be higher for stronger storms. The slowdown of inward travelling injections is indicative of braking as the bubble enters regions with decreasing difference in flux tube entropy. The average injection velocity is also generally higher for CIR-driven storms than CME-driven storms of similar strength.

Appendix A: Model Coupling Details

The coupling between the OpenGGCM and RCM, as detailed in the following paragraphs, is highly configurable through the use of input parameters. Table A1 lists the primary parameters, with the values used in this study.

Input MHD pressure on the 2-D RCM grid is calculated by using a flux tube volume-weighted average of the MHD pressure according to equations (A1) and (A2) along each cell's associated field line. Density is calculated in the same manner. The pressure and density on the RCM grid are then converted to flux tube content (η) on the boundary using equations (A3) and (A4), respectively. The RCM then executes normally.

$$p_{rcm} = \Sigma (w_i \cdot p_{mhd,i}) / \Sigma w_i \quad (A1)$$

$$w_i = \left(\frac{r_i - r_{min}}{r_{max} - r_{min}} \right) \frac{1}{B_i} \quad (A2)$$

$$p_k = \frac{2}{3} \frac{\eta_k \lambda_k}{V^{5/3}} \quad (A3)$$

$$n_k = \eta_k / V \quad (A4)$$

After RCM execution, the flux tube content is converted back to total pressure and density on the RCM grid by summing the contribution from all invariant energy levels. These values are interpolated to MHD 3-D cells by tracing magnetic field lines backward from the cell centers to the 2-D grid. When two-way feedback is enabled, these values are used to modify MHD pressure, density, and energy in the RCM domain according to equations (A5)–(A7) (the density calculation is similar to that of pressure; $B_{min,\eta}$ is the minimum B along the traced field line). This feedback ramps up from zero to 100% over the course of a configurable ramp-up period, where f_{fb} is slowly increased to its calculated value over time.

$$f_{fb} = \min \left(1, \left(\frac{B_{min,\eta} - B_{min}}{B_{ceil} - B_{min}} \right) \right) \quad (A5)$$

$$p_{mhd} = (1 - f_{fb}) p_{mhd} + f_{fb} \cdot p_{rcm} \quad (A6)$$

$$e_{mhd} = e_{mhd} + f_{fb} \frac{(p_{rcm} - p_{mhd})}{(\gamma - 1)} \quad (A7)$$

The coupling region between the OpenGGCM and RCM is defined by distance (r_{min}, r_{max}). However, a minimum magnetic field strength requirement (B_{min}) can move the outer boundary inward. Feedback is partially limited near the RCM outer boundary, with a linear drop-off from the location of magnetic field strength of B_{ceil} to the outer boundary. A combination of dipole and MHD-provided magnetic fields, where the dipole is used for the inner region and MHD field for the outer and the two are blended in the middle, is used to trace field lines from the RCM ionosphere grid through the MHD 3-D grid in order to exchange quantities between the models.

The initial execution of the RCM is delayed by a configurable amount of time after the OpenGGCM start time to allow the OpenGGCM to properly initialize. After this time, coupling is purely one way, with no feedback to the OpenGGCM. After another configurable delay, the RCM begins to feed pressure and density back to the MHD nodes. As stated previously, this feedback has a ramp-up period.

Table A1. RCM Feedback Parameters

Parameter	Value
RCM start (OpenGGCM time)	5400 s
RCM feedback start	7200 s
RCM feedback ramp-up duration	3600 s
r_{min} (lower coupling bound)	1.5 R_E
r_{max} (upper coupling bound)	10 R_E
B_{min} (min B allowed in coupling region)	30 nT
B_{ceil} (lower bound of limited feedback)	100 nT

As with RCM feedback to the MHD portions of the OpenGGCM, the contribution of RCM quantities during blending with ionosphere quantities is incrementally increased during the same ramp-up period.

Acknowledgments

This research was funded through NSF grants AGS-1303579 and AGS-1603021 and NASA grants NNX15AW16G and NNX13AK31G. Computations were performed on Trillian, a Cray XE6m-200 supercomputer at UNH supported by the NSF MRI program under grant PHY-1229408. We acknowledge the use of OMNI and Wind solar wind data through CDAWeb. We wish to thank Dick Wolf for his review of this manuscript. The simulation data of this paper are available upon request.

References

- Angelopoulos, V., W. Baumjohann, C. F. Kennel, F. V. Coroniti, M. G. Kivelson, R. Pellat, R. J. Walker, H. Luehr, and G. Paschmann (1992), Bursty bulk flows in the inner central plasma sheet, *J. Geophys. Res.*, *97*, 4027–4039, doi:10.1029/91JA02701.
- Angelopoulos, V., C. F. Kennel, F. V. Coroniti, R. Pellat, M. G. Kivelson, R. J. Walker, C. T. Russell, W. Baumjohann, W. C. Feldman, and J. T. Gosling (1994), Statistical characteristics of bursty bulk flow events, *J. Geophys. Res.*, *99*, 21,257–21,280, doi:10.1029/94JA01263.
- Baumjohann, W. (2002), Modes of convection in the magnetotail, *Phys. Plasmas*, *9*, 3665–3667, doi:10.1063/1.1499116.
- Baumjohann, W., G. Paschmann, and H. Luehr (1990), Characteristics of high-speed ion flows in the plasma sheet, *J. Geophys. Res.*, *95*, 3801–3809, doi:10.1029/JA095iA04p03801.
- Birn, J., and M. Hesse (1996), Details of current disruption and diversion in simulations of magnetotail dynamics, *J. Geophys. Res.*, *101*, 15,345–15,358, doi:10.1029/96JA00887.
- Birn, J., J. Raeder, Y. Wang, R. Wolf, and M. Hesse (2004), On the propagation of bubbles in the geomagnetic tail, *Ann. Geophys.*, *22*, 1773–1786, doi:10.5194/angeo-22-1773-2004.
- Birn, J., R. Nakamura, E. V. Panov, and M. Hesse (2011), Bursty bulk flows and dipolarization in MHD simulations of magnetotail reconnection, *J. Geophys. Res.*, *116*, A01210, doi:10.1029/2010JA016083.
- Buzulukova, N., M.-C. Fok, A. Pulkkinen, M. Kuznetsova, T. E. Moore, A. Gloer, P. C. Brandt, G. Tóth, and L. Rastätter (2010), Dynamics of ring current and electric fields in the inner magnetosphere during disturbed periods: CRCM-BATS-R-US coupled model, *J. Geophys. Res.*, *115*, A05210, doi:10.1029/2009JA014621.
- Chen, C. X., and R. A. Wolf (1999), Theory of thin-filament motion in Earth's magnetotail and its application to bursty bulk flows, *J. Geophys. Res.*, *104*, 14,613–14,626, doi:10.1029/1999JA900005.
- de Zeeuw, D. L., S. Sazykin, R. A. Wolf, T. I. Gombosi, A. J. Ridley, and G. Tóth (2004), Coupling of a global MHD code and an inner magnetospheric model: Initial results, *J. Geophys. Res.*, *109*, A12219, doi:10.1029/2003JA010366.
- Dubyagin, S., V. Sergeev, S. Apatenkov, V. Angelopoulos, A. Runov, R. Nakamura, W. Baumjohann, J. McFadden, and D. Larson (2011), Can flow bursts penetrate into the inner magnetosphere?, *Geophys. Res. Lett.*, *38*, L08102, doi:10.1029/2011GL047016.
- Dungey, J. W. (1961), Interplanetary magnetic field and the auroral zones, *Phys. Rev. Lett.*, *6*, 47–48, doi:10.1103/PhysRevLett.6.47.
- Erickson, G. M., and R. A. Wolf (1980), Is steady convection possible in the Earth's magnetotail, *Geophys. Res. Lett.*, *7*, 897–900, doi:10.1029/GL007i011p00897.
- Fenrich, F. R., and J. G. Luhmann (1998), Geomagnetic response to magnetic clouds of different polarity, *Geophys. Res. Lett.*, *25*(15), 2999–3002, doi:10.1029/98GL51180.
- Fok, M.-C., T. E. Moore, P. C. Brandt, D. C. Delcourt, S. P. Slinker, and J. A. Fedder (2006), Impulsive enhancements of oxygen ions during substorms, *J. Geophys. Res.*, *111*, A10222, doi:10.1029/2006JA011839.
- Fuller-Rowell, T. J., D. Rees, S. Quegan, R. J. Moffett, M. V. Codrescu, and G. H. Millward (1996), A Coupled Thermosphere-Ionosphere Model (CTIM), in *STEP: Handbook of Ionospheric Models*, edited by R. W. Schunk, p. 217, Scientif. Commit. on Sol. Terr. Phys. (SCOSTEP), NOAA/NGDC, Boulder, Colo.
- Gabrielse, C., V. Angelopoulos, A. Runov, and D. L. Turner (2012), The effects of transient, localized electric fields on equatorial electron acceleration and transport toward the inner magnetosphere, *J. Geophys. Res.*, *117*, A10213, doi:10.1029/2012JA017873.
- Ge, Y. S., J. Raeder, V. Angelopoulos, M. L. Gilson, and A. Runov (2011), Interaction of dipolarization fronts within multiple bursty bulk flows in global MHD simulations of a substorm on 27 February 2009, *J. Geophys. Res.*, *116*, A00123, doi:10.1029/2010JA015758.
- Gloer, A., M. Fok, X. Meng, G. Toth, N. Buzulukova, S. Chen, and K. Lin (2013), CRCM + BATS-R-US two-way coupling, *J. Geophys. Res. Space Physics*, *118*, 1635–1650, doi:10.1002/jgra.50221.
- Hu, B., F. R. Toffoletto, R. A. Wolf, S. Sazykin, J. Raeder, D. Larson, and A. Vapirev (2010), One-way coupled OpenGGCM/RCM simulation of the 23 March 2007 substorm event, *J. Geophys. Res.*, *115*, A12205, doi:10.1029/2010JA015360.
- Huang, C. Y., and L. A. Frank (1986), A statistical study of the central plasma sheet: Implications for substorm models, *Geophys. Res. Lett.*, *13*, 652–655, doi:10.1029/GL013i007p00652.
- Juusola, L., N. Østgaard, and E. Tanskanen (2011), Statistics of plasma sheet convection, *J. Geophys. Res.*, *116*, A08201, doi:10.1029/2011JA016479.
- Keika, K., et al. (2009), Observations of plasma vortices in the vicinity of flow-braking: A case study, *Ann. Geophys.*, *27*, 3009–3017, doi:10.5194/angeo-27-3009-2009.
- Kim, H.-S., D.-Y. Lee, S. Ohtani, M.-Y. Park, and B.-H. Ahn (2012), On near-tail bubble penetration into geosynchronous altitude, *J. Geophys. Res.*, *117*, A07205, doi:10.1029/2012JA017749.
- Lemon, C., R. A. Wolf, T. W. Hill, S. Sazykin, R. W. Spiro, F. R. Toffoletto, J. Birn, and M. Hesse (2004), Magnetic storm ring current injection modeled with the Rice Convection Model and a self-consistent magnetic field, *Geophys. Res. Lett.*, *31*, L21801, doi:10.1029/2004GL020914.
- Liu, J., V. Angelopoulos, X.-Z. Zhou, and A. Runov (2014), Magnetic flux transport by dipolarizing flux bundles, *J. Geophys. Res. Space Physics*, *119*, 909–926, doi:10.1002/2013JA019395.
- McPherron, R. L., T.-S. Hsu, J. Kissinger, X. Chu, and V. Angelopoulos (2011), Characteristics of plasma flows at the inner edge of the plasma sheet, *J. Geophys. Res.*, *116*, A00133, doi:10.1029/2010JA015923.
- Meng, X., G. Tóth, A. Gloer, M.-C. Fok, and T. I. Gombosi (2013), Pressure anisotropy in global magnetospheric simulations: Coupling with ring current models, *J. Geophys. Res. Space Physics*, *118*, 5639–5658, doi:10.1002/jgra.50539.
- Moore, T. E., M.-C. Fok, D. C. Delcourt, S. P. Slinker, and J. A. Fedder (2008), Plasma plume circulation and impact in an MHD substorm, *J. Geophys. Res.*, *113*, A06219, doi:10.1029/2008JA013050.
- Nakamura, R., et al. (2004), Spatial scale of high-speed flows in the plasma sheet observed by Cluster, *Geophys. Res. Lett.*, *31*, L09804, doi:10.1029/2004GL019558.
- Ohtani, S.-I., M. A. Shay, and T. Mukai (2004), Temporal structure of the fast convective flow in the plasma sheet: Comparison between observations and two-fluid simulations, *J. Geophys. Res.*, *109*, A03210, doi:10.1029/2003JA010002.
- Panov, E. V., et al. (2010), Multiple overshoot and rebound of a bursty bulk flow, *Geophys. Res. Lett.*, *37*, L08103, doi:10.1029/2009GL041971.
- Pembroke, A., F. Toffoletto, S. Sazykin, M. Wiltberger, J. Lyon, V. Merkin, and P. Schmitt (2012), Initial results from a dynamic coupled magnetosphere-ionosphere-ring current model, *J. Geophys. Res.*, *117*, A02211, doi:10.1029/2011JA016979.
- Pontius, D. H. Jr., and R. A. Wolf (1990), Transient flux tubes in the terrestrial magnetosphere, *Geophys. Res. Lett.*, *17*, 49–52, doi:10.1029/GL017i001p00049.

- Raeder, J., D. Larson, W. Li, E. L. Kepko, and T. Fuller-Rowell (2008), OpenGGCM simulations for the THEMIS mission, *Space Sci. Rev.*, *141*, 535–555, doi:10.1007/s11214-008-9421-5.
- Runov, A., V. Angelopoulos, X.-Z. Zhou, X.-J. Zhang, S. Li, F. Plaschke, and J. Bonnell (2011), A THEMIS multicase study of dipolarization fronts in the magnetotail plasma sheet, *J. Geophys. Res.*, *116*, A05216, doi:10.1029/2010JA016316.
- Runov, A., V. Angelopoulos, C. Gabrielse, J. Liu, D. L. Turner, and X.-Z. Zhou (2015), Average thermodynamic and spectral properties of plasma in and around dipolarizing flux bundles, *J. Geophys. Res. Space Physics*, *120*, 4369–4383, doi:10.1002/2015JA021166.
- Schmid, D., et al. (2016), A comparative study of dipolarization fronts at MMS and Cluster, *Geophys. Res. Lett.*, *43*, 6012–6019, doi:10.1002/2016GL069520.
- Schödel, R., W. Baumjohann, R. Nakamura, V. A. Sergeev, and T. Mukai (2001), Rapid flux transport in the central plasma sheet, *J. Geophys. Res.*, *106*, 301–314, doi:10.1029/2000JA900139.
- Semenov, V. S., T. Penz, V. V. Ivanova, V. A. Sergeev, H. K. Biernat, R. Nakamura, M. F. Heyn, I. V. Kubyshkin, and I. B. Ivanov (2005), Reconstruction of the reconnection rate from Cluster measurements: First results, *J. Geophys. Res.*, *110*, A11217, doi:10.1029/2005JA011181.
- Sergeev, V. A., V. Angelopoulos, J. T. Gosling, C. A. Cattell, and C. T. Russell (1996), Detection of localized, plasma-depleted flux tubes or bubbles in the midtail plasma sheet, *J. Geophys. Res.*, *101*, 10,817–10,826, doi:10.1029/96JA00460.
- Shiokawa, K., W. Baumjohann, and G. Haerendel (1997), Braking of high-speed flows in the near-Earth tail, *Geophys. Res. Lett.*, *24*, 1179–1182, doi:10.1029/97GL01062.
- Toffoletto, F., S. Sazykin, R. Spiro, and R. Wolf (2003), Inner magnetospheric modeling with the Rice Convection Model, *Space Sci. Rev.*, *107*, 175–196, doi:10.1023/A:1025532008047.
- Toffoletto, F. R., S. Sazykin, R. W. Spiro, R. A. Wolf, and J. G. Lyon (2004), RCM meets LFM: Initial results of one-way coupling, *J. Atmos. Sol. Terr. Phys.*, *66*, 1361–1370, doi:10.1016/j.jastp.2004.03.022.
- Tsyganenko, N. A., and T. Mukai (2003), Tail plasma sheet models derived from Geotail particle data, *J. Geophys. Res.*, *108*, 1136, doi:10.1029/2002JA009707.
- Vasyliunas, V. M. (1970), Mathematical models of magnetospheric convection and its coupling to the ionosphere, in *Particles and Field in the Magnetosphere, Astrophysics and Space Science Library*, vol. 17, edited by B. M. McCormack and A. Renzini, pp. 60–71, Springer, Netherlands.
- Welling, D. T., V. K. Jordanova, A. Gloer, G. Toth, M. W. Liemohn, and D. R. Weimer (2015), The two-way relationship between ionospheric outflow and the ring current, *J. Geophys. Res. Space Physics*, *120*, 4338–4353, doi:10.1002/2015JA021231.
- Wiltberger, M., V. Merkin, J. G. Lyon, and S. Ohtani (2015), High-resolution global magnetohydrodynamic simulation of bursty bulk flows, *J. Geophys. Res. Space Physics*, *120*, 4555–4566, doi:10.1002/2015JA021080.
- Wolf, R. A. (1983), The quasi-static (slow-flow) region of the magnetosphere, in *Solar-Terrestrial Physics: Principles and Theoretical Foundations, Astrophysics and Space Science Library*, vol. 104, edited by R. L. Carovillano and J. M. Forbes, pp. 303–368, D. Reidel, Dordrecht, Netherlands.
- Wolf, R. A., Y. Wan, X. Xing, J.-C. Zhang, and S. Sazykin (2009), Entropy and plasma sheet transport, *J. Geophys. Res.*, *114*, A00D05, doi:10.1029/2009JA014044.
- Wolf, R. A., C. X. Chen, and F. R. Toffoletto (2012), Thin filament simulations for Earth's plasma sheet: Interchange oscillations, *J. Geophys. Res.*, *117*, A02215, doi:10.1029/2011JA016971.
- Yang, J., F. R. Toffoletto, R. A. Wolf, and S. Sazykin (2011), RCM-E simulation of ion acceleration during an idealized plasma sheet bubble injection, *J. Geophys. Res.*, *116*, A05207, doi:10.1029/2010JA016346.
- Yang, J., F. R. Toffoletto, X. Xing, and V. Angelopoulos (2012), RCM-E simulation of the 13 March 2009 steady magnetospheric convection event, *J. Geophys. Res.*, *117*, A03224, doi:10.1029/2011JA017245.
- Yang, J., F. R. Toffoletto, R. A. Wolf, and S. Sazykin (2015), On the contribution of plasma sheet bubbles to the storm time ring current, *J. Geophys. Res. Space Physics*, *120*, 7416–7432, doi:10.1002/2015JA021398.
- Yang, J., F. R. Toffoletto, and R. A. Wolf (2016), Comparison study of ring current simulations with and without bubble injections, *J. Geophys. Res. Space Physics*, *121*, 374–379, doi:10.1002/2015JA021901.
- Yao, Z. H., et al. (2015), A physical explanation for the magnetic decrease ahead of dipolarization fronts, *Ann. Geophys.*, *33*, 1301–1309, doi:10.5194/angeo-33-1301-2015.
- Yu, Y., V. Jordanova, D. Welling, B. Larsen, S. G. Claudepierre, and C. Kletzing (2014), The role of ring current particle injections: Global simulations and Van Allen Probes observations during 17 March 2013 storm, *Geophys. Res. Lett.*, *41*, 1126–1132, doi:10.1002/2014GL059322.
- Zaharia, S., V. K. Jordanova, M. F. Thomsen, and G. D. Reeves (2008), Self-consistent geomagnetic storm simulation: The role of the induced electric fields, *J. Atmos. Sol. Terr. Phys.*, *70*, 511–518, doi:10.1016/j.jastp.2007.08.067.
- Zhang, J.-C., R. A. Wolf, S. Sazykin, and F. R. Toffoletto (2008), Injection of a bubble into the inner magnetosphere, *Geophys. Res. Lett.*, *35*, L02110, doi:10.1029/2007GL032048.